

Layer Control of Magneto-Optical Effects and Their Quantization in Spin-Valley Splitting Antiferromagnets

Jiaqi Feng, Xiaodong Zhou,* Meiling Xu, Jingming Shi, and Yinwei Li*

*Laboratory of Quantum Functional Materials Design and Application, School of Physics
and Electronic Engineering, Jiangsu Normal University, Xuzhou 221116, China*

E-mail: xdzhou323@gmail.com; yinwei_li@jsnu.edu.cn

Abstract

Magneto-optical effects (MOE), interfacing the fundamental interplay between magnetism and light, have served as a powerful probe for magnetic order, band topology, and valley index. Here, based on multiferroic and topological bilayer antiferromagnets (AFMs), we propose a layer control of MOE (L-MOE), which is created and annihilated by layer-stacking or an electric field effect. The key character of L-MOE is the sign-reversible response controlled by ferroelectric polarization, the Néel vector, or the electric field direction. Moreover, the sign-reversible L-MOE can be quantized in topologically insulating AFMs. We reveal that the switchable L-MOE originates from the combined contributions of spin-conserving and spin-flip interband transitions in spin-valley splitting AFMs, a phenomenon not observed in conventional AFMs. Our findings bridge the ancient MOE to the emergent realms of layertronics, valleytronics, and multiferroics, and may hold immense potential in these fields.

Keywords

layer-spin-valley, magneto-optical effects, multiferroic, topological antiferromagnets

Magneto-optical Kerr¹ and Faraday² effects (MOKE, MOFE), referring to the change of polarization plane of light reflecting from and transmitting through a magnetic material, respectively (see Figure 1), offer prominent benefits for basic science and technology applications.³⁻⁶ As a modern noncontact spectroscopic technique, magneto-optical effects (MOE) manifest itself as a powerful tool for measuring magnetic order in two-dimensional (2D) materials, overcoming inevitable difficulties using standard techniques from superconducting quantum interference device and neutron scattering, as successfully performed in CrI₃,⁷ Cr₂Ge₂Te₆,⁸ and Fe₃GeTe₂.⁹ Besides, MOE have also matured into a sophisticated probe for exploring band topology¹⁰⁻¹³ and valley index.^{14,15}

The common MOE arises from the combined effects of band exchange splitting (induced by a finite net magnetization) and spin-orbit coupling (SOC).³⁻⁵ Antiferromagnets (AFMs), appear to pose a challenge for hosting MOE due to the absence of a net magnetization and usually suffer from the limitation from usual Kramers double band degeneracy. However, this empirical knowledge was questioned by several recent theoretical and experimental progresses in certain noncollinear AFMs. Feng *et al.*¹⁶ first revealed an unexpected MOE in coplanar noncollinear AFMs Mn₃X (X = Rh, Ir, Pt) with special vector-spin chirality, which is also the cases for other kinds of noncollinear AFMs Mn₃ZN (Z = Ga, Zn, Ag, Ni)¹⁷ and Mn₃Y (Y = Ge, Ga, Sn).¹⁸ The MOE in noncollinear AFMs was soon experimentally confirmed in Mn₃Sn^{19,20} and Mn₃Ge.²¹ Subsequently, Feng *et al.*²² further proposed a novel (quantum) topological MOE in noncoplanar AFMs, which stems from a finite scalar spin chirality and emerges even without SOC and band exchange splitting simultaneously, thus reshaping our understandings of the MOE. Very recently, the topological MOE was observed experimentally in skyrmion lattice.²³

These advances indicate that the MOE is essentially controlled by magnetic symmetry,²⁵ with its symmetry rules traceable to the ac Hall pseudovector $\boldsymbol{\sigma}(\omega) = [\sigma_{yz}(\omega), \sigma_{zx}(\omega), \sigma_{xy}(\omega)]$.²⁶ The conventional collinear AFMs usually host \mathcal{TP} or $\mathcal{T}\tau$ symmetry (\mathcal{T} is the time-reversal; \mathcal{P} is spatial inversion, and τ is lattice translation). The tensor $\boldsymbol{\sigma}$ is invariant under lattice

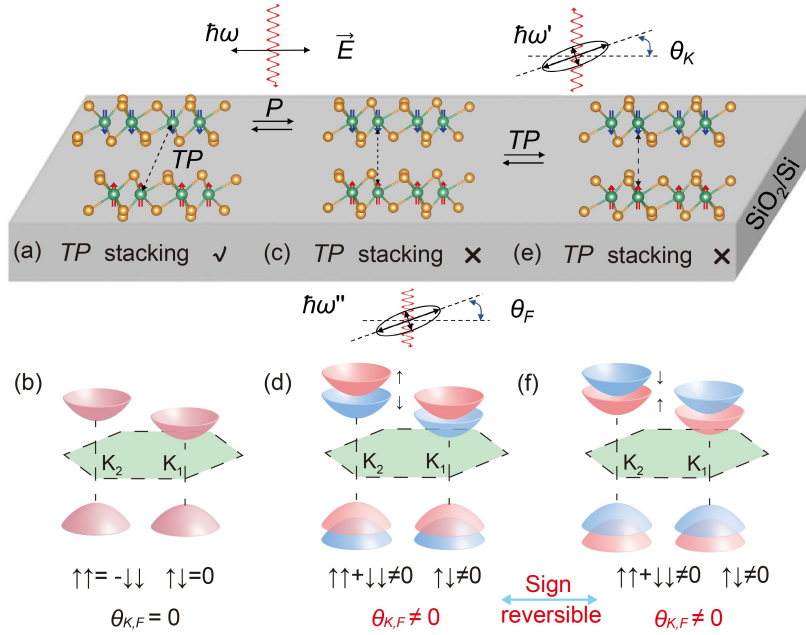


Figure 1: Schematic illustration of L-MOE in spin-valley splitting AFMs. (a-b) The vanishing MOE with conventional \mathcal{TP} -symmetric layer stacking. The system exhibits a valley-polarized property, while it still obeys the Kramers spin degeneracy theorem. In this case, the interband optical transition between the spin-up valley and the spin-up valley ($\uparrow\uparrow$) tends to cancel out that of the time-reversal symmetric transition from the spin-down valley to the spin-down valley ($\downarrow\downarrow$). Moreover, the transition between states with opposite spins (spin-flip, $\uparrow\downarrow$) is forbidden. (c-d) After breaking the \mathcal{TP} symmetry via a layer-stacking effect [e.g., from (a) to (c) by rearranging the top layer under a \mathcal{P} operation], the spin degeneracy is further lifted. The combined spin-valley polarization permits the optical excitation from both the spin-conserving ($\uparrow\uparrow + \downarrow\downarrow \neq 0$) and spin-flip transitions ($\uparrow\downarrow \neq 0$). Interestingly, the sign of the L-MOE is reversible by flipping the spin-splitting bands [e.g., from (d) to (f)], which can be achieved by reversing the ferroelectric polarization or Néel vector direction [e.g., from (c) to (e) by rearranging the bilayer under a \mathcal{TP} operation]. Moreover, the sign-reversible L-MOE can be also excited in conventional \mathcal{TP} -symmetric AFMs under a vertical electric field, sharing the similar physics to the novel dc case of layer Hall effect.²⁴

translation. While with respect to \mathcal{T} (\mathcal{P}) symmetry, the σ is odd (even) function. Thus, the combined \mathcal{TP} or $\mathcal{T}\tau$ can force the σ to be zero and lead to vanishing MOE. For a 2D system ($\sigma_{yz} = 0$, $\sigma_{zx} = 0$), the MOE is also suppressed by some \mathcal{O} symmetries [e.g., \mathcal{O} may be \mathcal{M}_x , \mathcal{M}_y , C_{2x} , and C_{2y}] as well as limited by some combined \mathcal{TS} symmetries [e.g., \mathcal{S} may be \mathcal{M}_z , C_{2z} , C_{3z} , C_{4z} , C_{6z}] due to the odd property of σ_{xy} under these symmetries.²⁵ Hence, by breaking above symmetries, MOE may also emerge in more commonly available collinear AFMs.²⁵⁻³³ From the nanoscience application perspective, it is much desirable to enrich the MOE family in 2D collinear AFMs because of the emergent valley-indexes,³⁴⁻⁴¹ layer physics,^{24,42-48} and multiferroic order.⁴⁹⁻⁵⁵ Importantly, it is highly desirable to realize the long-sought spin-splitting in 2D AFMs, which has triggered extensive attention recently benefiting from the versatile development of altermagnetism.⁵⁶⁻⁵⁸

In this work, we propose a layer control of MOE (L-MOE) in multiferroic bilayer Nb_3I_8 and topological bilayer MnBi_2Te_4 . The L-MOE is switched on and off by a layer stacking effect, depending on whether the \mathcal{TP} symmetry is broken [Figure 1(c)-(d)] or not [Figure 1(a)-(b)]. The presence of L-MOE originates from the combined spin-valley-splitting in AFMs [Figure 1(d)], which enables the nonzero contributions from both the spin-conserving ($\uparrow\uparrow + \downarrow\downarrow$) and spin-flip ($\uparrow\downarrow$) interband optical transitions. The spin-flip process is usually prohibited by the optical selection rule while it can be aroused in spin-splitting systems when considering the SOC effect.⁵⁸⁻⁶⁷ It can be served as a unique hallmark for spin-valley splitting AFMs, a phenomenon absent in conventional \mathcal{TP} -symmetric AFMs due to the time-reversal symmetric interband transitions between states of opposing spins [$\uparrow\uparrow = -\downarrow\downarrow$, Figure 1(b)]. The typical character of L-MOE is that its sign is reversible by reversing the ferroelectric polarization or Néel vector directions [Figure 1(c)-(f)]. Moreover, we reveal that the sign-reversible L-MOE can be also excited in the \mathcal{TP} -symmetric AFMs by an electric field effect, presenting the similar physics to the novel dc case of layer Hall effect.²⁴ Interestingly, this sign-reversible L-MOE can be quantized in insulating topological bilayer antiferromagnets in the low-frequency limit. Our findings integrate the properties of emergent layer, spin, valley,

ferroelectricity, and topology into the MOE and suggest a promising platform for spintronic, valleytronic, multiferroic, and magneto-optical applications.

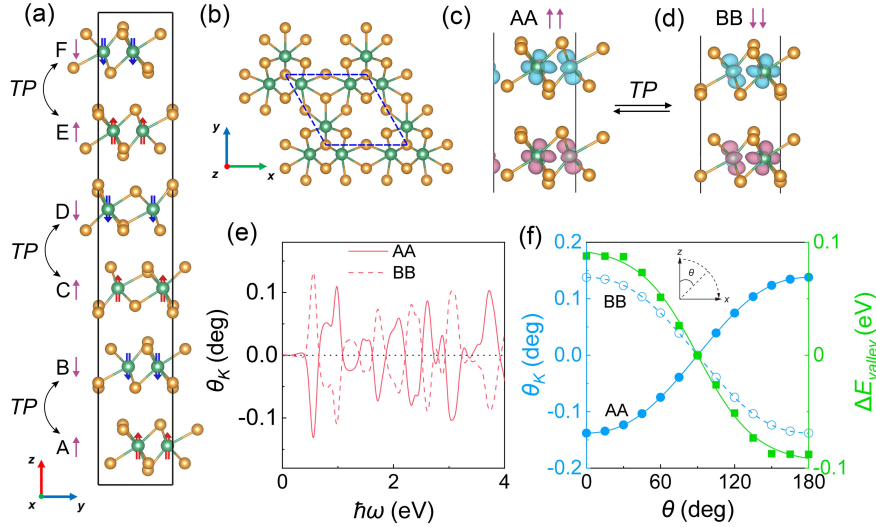


Figure 2: Sign-reversible L-MOE in multiferroic bilayer AFMs. (a) Side view of A-type antiferromagnetic bulk Nb_3I_8 , labeled A-F from bottom to top layer, and (b) top view of monolayer Nb_3I_8 . The red and blue arrows in (a) denote the magnetization direction. The A(C, E) and B(D, F) layers in the A-type antiferromagnetic bulk crystal are related to each other by a \mathcal{TP} symmetry. The blue dash lines in (b) denote the primitive cell. (c-d) Side views of magnetic density isosurfaces for bilayer AA and BB stacked Nb_3I_8 , which are related to each other by a \mathcal{TP} symmetry and have an opposite ferroelectric polarization directions. The purple arrows in (a) and (c-d) indicate the polarization direction. The green and yellow balls in (a-d) represent Nb and I atoms, respectively. (e) L-MOE of bilayer Nb_3I_8 in AA and BB staking. (f) Angle evolution of maximum Kerr rotation angle (blue symbols and lines) and valley-splitting ΔE_{valley} (green symbols and lines) for AA and BB stacking. The ΔE_{valley} is defined as the energy difference between two K valley at the conduction band edge [see Figure 4(g) and (l)].

The layered transition metal halides Nb_3X_8 ($X = \text{Cl}, \text{Br}, \text{I}$) have attracted increasing interest due to its exotic layered magnetic kagome lattice, topological flat bands, and transport properties.^{68–82} Recently, the monolayer and few layers Nb_3I_8 were cleaved mechanically from the bulk crystal.^{70,71} There are six monolayers in the bulk Nb_3I_8 with a stacking order of A-B-C-D-E-F along the c direction [see Figure 2(a)]. Each layer hosts a breathing kagome lattice constructed by magnetic Nb trimers which are coordinated by the distorted non-magnetic I octahedron environment, as shown in Figure 2(b). Such an arrangement breaks inversion symmetry from space group of $P3m1$ and exhibits a spontaneous valley polariza-

tion⁷³ as well as ferroelectric polarization along the out-of-plane direction.^{77,78} Among these, the A, C, and E monolayers are interconnected through a lattice translation operation. They have ferroelectric polarization along the z direction. The B (D, F) and A (C, E) layers are related to each other by an inversion symmetry (without considering magnetism). So, the ferroelectric polarization direction of B, D, and F monolayers is along the $-z$ direction, which are revealed by recent theoretical and experimental reports.^{77,78} While the magnetism of Nb_3I_8 has yet to be measured experimentally, several preceding theoretical works have forecasted its layer-dependent magnetic properties,⁷²⁻⁷⁷ e.g., ferromagnetism for monolayer and antiferromagnetism for bilayer. By comparing the total energies among the ferromagnetic, nonmagnetic, and different antiferromagnetic states [see Figures S1-S2 and Tables S1-S2], we find that the bulk and monolayer Nb_3I_8 prefer to a A-type antiferromagnetic ground state [see Figure 2(a)] and ferromagnetic ground state, respectively, which is in accordance with the prior studies.⁷²⁻⁷⁷ The optimized lattice constants of monolayer, bulk crystal, and bilayers are shown in Table S1-S3, which are in reasonable agreement with the experimental results.^{68,69}

The key findings of L-MOE are demonstrated in the bilayer multiferroic Nb_3I_8 . The previous studies^{77,78} suggest that the two layers with same (opposite) polarization directions are the ferroelectric (antiferroelectric) states. For example, the AA (CC, EE) bilayer hosts the ferroelectric polarization along the z direction, while the BB (DD, FF) being along the $-z$ direction [see Figure 2(c)-(d)], respectively. Correspondingly, the AB (BC, CD, DE, and EF) layer stacking is the antiferroelectric state. By layer sliding and twisting, one can obtain more abundant multiferroic states in bilayer Nb_3I_8 . Here, we consider seven simplest stacking configurations such as AA(BB), AB, AC, AD, AE, and AF, which are sufficient to reveal the L-MOE in the following discussion. The magnetic ground states of AD and AE prefer to interlayer ferromagnetic coupling, while AA (BB), AB, AC, and AF feature an interlayer A-type antiferromagnetic coupling, showing a strong stacking-dependent magnetism which is also reported in bilayer CrI_3 ⁸³ and MnBi_2Te_4 .⁴³ Next, we will focus on

bilayer antiferromagnetic AA (BB), AB, AC, and AF stacking to reveal the sign-reversible L-MOE.

First, the basic property of sign-reversible L-MOE is demonstrated directly based on the magnetization density and magnetic group analyses. Figure 2(c) shows the magnetization density of bilayer AA stacking, the usual \mathcal{TP} , \mathcal{TS} , and \mathcal{O} symmetries that suppress the MOE are broken apparently. In this case, the σ_{xy} or L-MOE is nonzero protected by the magnetic point group of $3m'1$. Interestingly, the ferroelectric counterpart of BB stacking has a degenerate energy and same magnetic point group as the AA stacking, while their magnetic density isosurfaces are connected by a \mathcal{TP} transformation [see Figure 2(c) and (d)]. The MOE is odd and even with respect to \mathcal{T} and \mathcal{P} symmetries, respectively. Therefore, the two opposite antiferromagnetic ferroelectric states (AA and BB) must have a reverse sign of L-MOE. This sign-reversible principle can also be extended into all other paired ferroelectric states of bilayer Nb_3I_8 with opposite polarization directions. The magnetic group analyses are further confirmed by the first-principles results. The Figure 2(e) presents a long-sought MOE in AA- and BB-stacked antiferromagnetic Nb_3I_8 with the Néel vector being along the z direction. The largest Kerr rotation angle of about 0.13° is comparable to the typical magnitude of $0^\circ \sim 2^\circ$ in some usual layered magnets, such as CrI_3 ,⁸⁴ $\text{Cr}_2\text{Ge}_2\text{Te}_6$,⁸⁵ Fe_nGeTe_2 ($n = 3, 4, 5$),⁸⁶ CrTe_2 ,⁸⁷ and CrSBr .⁸⁸ As expected from symmetry analyses, the AA and BB stacking with opposite ferroelectric polarization directions exhibit the same magnitude but opposite sign of L-MOE.

Besides the induced sign-reversible response, the layer stacking also plays a significant role in the presence and absence of L-MOE in bilayer Nb_3I_8 . The L-MOE of AB and AF stacking are vanishing because the systems possess a \mathcal{TP} symmetry from a magnetic point group of $\bar{3}'1m'$. While for AC stacking, the L-MOE is allowed due to the same magnetic point group $3m'1$ as the AA stacking. The first-principles calculations indeed reproduce the results of symmetry analyses. Figure 3(a-b) shows the magneto-optical Kerr and Faraday rotation angles $\theta_{K,F}$ for different layer stacking. Apparently, the $\theta_{K,F}$ for AB and AF stacking

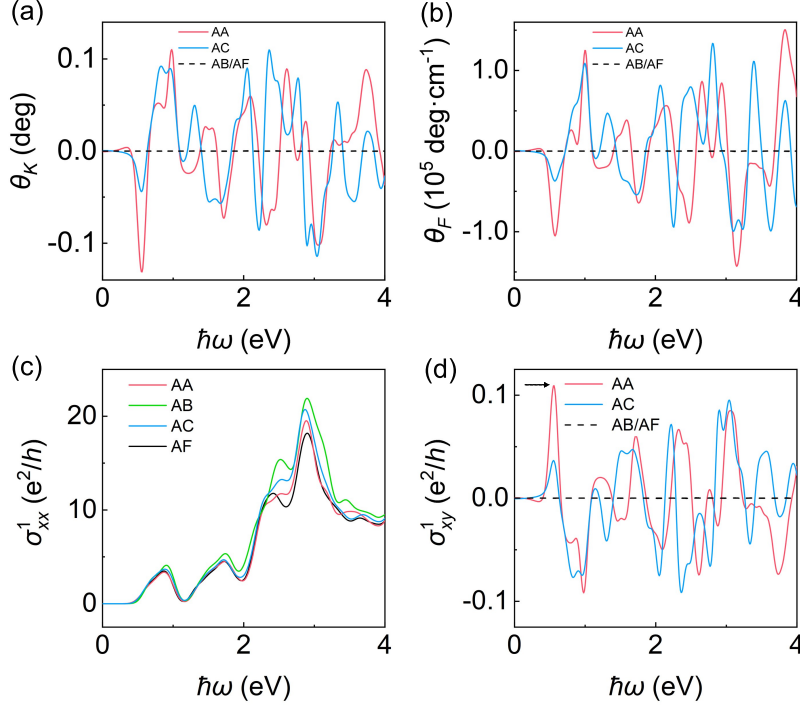


Figure 3: Layer-stacking dependent L-MOE in bilayer AFMs. (a-b) MOKE and MOFE, (c-d) real parts of diagonal element σ_{xx} and off-diagonal element σ_{xy} , for bilayer antiferromagnetic Nb_3I_8 with different stacking. The arrow in (d) marks the maximum of σ_{xy}^1 .

are equal to zero in the whole frequency range, while it is nonvanishing for AA and AC stacking. One can also observe that the magnitudes of L-MOE are substantially affected by layer stacking. This novel phenomenon is essentially controlled by the off-diagonal element σ_{xy} rather than diagonal element σ_{xx} of optical conductivity. The former (latter) depends significantly on (is robust against) layer stacking, as shown in Figure 3(c-d).

Taking the AA, BB, and AB stackings as typical examples, we now elucidate the underlying physics of the presence/absence of L-MOE and their sign-reversible response at the microscopic level based on the electronic structure calculations. Figure 4(a) and (b) show the spin-polarized and relativistic band structures of AB stacking with the Néel vector being along the z direction, respectively. Without SOC, one clearly observes that the AB stacking obeys Kramers spin degeneracy with a pair of degenerate valleys at K_1 and K_2 for both conduction and valence band edges. After considering the SOC effect, the double band degeneracy still exists due to the \mathcal{TP} symmetry, while the valley degeneracy is broken due

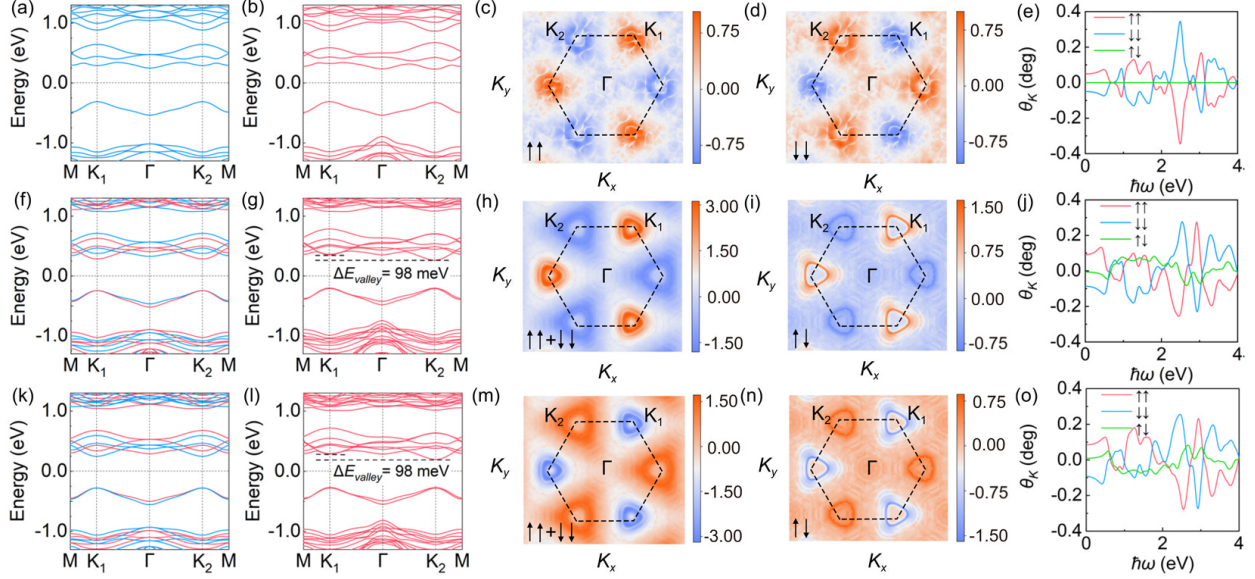


Figure 4: Underlying physical origin of sign-reversible L-MOE. (a, b)/(f, g) Spin-polarized and relativistic band structures of bilayer Nb_3I_8 with AB/AA stacking, respectively. (c, d) Momentum-resolved σ_{xy}^1 for AB stacking with the interband optical transitions between the bands from spin-up to spin-up ($\uparrow\uparrow$), and spin-down to spin-down ($\downarrow\downarrow$), respectively. (h, i) Similar to (c, d) but from spin-conserving ($\uparrow\uparrow + \downarrow\downarrow$) and spin-flip ($\uparrow\downarrow$) interband transitions. (e)/(j) Spin-resolved L-MOE with AB/AA stacking contributed from the interband transitions of $\uparrow\uparrow$, $\downarrow\downarrow$, and spin flip $\uparrow\downarrow$, respectively. (k-o) Similar to (f-j) but with BB stacking. In (c, d), (h, i) and (m, n), the σ_{xy}^1 (in units of e^2/h) is calculated at $\hbar\omega = 0.56$ eV and is marked by a black arrow in Figure 3(d). The reduced coordinates for the Berry curvature slice and high-symmetry points are shown in Figure S9.

to the novel coupled spin-valley physics.⁸⁹ By decomposing the interband optical transitions between the bands of the same spins (namely, spin-conserved parts $\uparrow\uparrow$ or $\downarrow\downarrow$) and the opposite spins (namely, spin-flip process $\uparrow\downarrow$), one can see that the momentum-resolved σ_{xy}^1 for spin-up to spin up ($\uparrow\uparrow$) and spin-down to spin-down ($\downarrow\downarrow$) interband transitions present a reverse distributions around two K valleys [see Figure 4(c) and (d)]. Thus, for this conventional AFM, the magneto-optical spectra from spin-conserved parts are cancelled out from each other, as shown in Figure 4(e), accompanying with a negligible contribution from the spin-flip process.

Nevertheless, a novel L-MOE is generated in AA stacking due to the lifted spin together with valley degeneracy, as revealed in the following discussion. Figure 4(f) and (g) show the spin-polarized and relativistic band structures of AA stacking with the Néel vector being

along the z direction, respectively. It is obvious that the Kramers spin degeneracy is lifted in the entire Brillouin zone even in this fully compensated collinear AFM, in contrast to the spin-momentum locking property in altermagnet.^{56–58} Therefore, the multiferroic bilayer Nb₃I₈ can also host the spin-polarized property of ferromagnets coupled with the extraordinary advantages of antiferromagnetic spin order such as ultrafast spin dynamics and without parasitic stray fields. The SOC effect further breaks the degeneracy of two K valleys. The valley splitting ΔE_{valley} can reach up to 98 meV at the conduction band edge, which is on the order of usual ferrovalley materials, such as monolayer Nb₃I₈,⁷³ VSe₂ or VS₂,^{37,52} VSi₂N₄ or VSi₂P₄.^{40,41,90–93} In contrast to \mathcal{TP} -symmetric antiferromagnetic materials, Figure 4(h) shows that the spin-conserving interband transitions ($\uparrow\uparrow+\downarrow\downarrow$) present an asymmetric distribution near two K valleys, which means the $\uparrow\uparrow$ component can not cancel out the $\downarrow\downarrow$ contribution. Notably, a finite spin-flip contribution emerges and also exhibits an unbalanced distributions around two K valleys [see Figure 4(i)], which is usually negligible small in most materials because the SOC energy scale is usually smaller than the exchange splitting energy scale.^{58–67} The nonvanishing contributions both from spin-conserving and spin-flip processes, induced by the strong SOC effect and special spin-splitting, ultimately give rise to a measurable L-MOE, as shown in Figure 4(j). One can see that the novel spin-flip process can be served as a unique marker for spin-valley splitting AFMs, which is absent for conventional \mathcal{TP} -symmetric AFMs. The sign-reversible magneto-optical response for AA and BB stacking can be also elucidated based on the spin-valley splitting physics. Figure 4(k)-(l) shows the spin-polarized and relativistic band structures for BB stacking. Apparently, they can be regarded as the time-reversal-like counterpart of the case in AA stacking. The σ_{xy} and MOE are all odd under time-reversal symmetry. Therefore, the signs for all of them are reversed when the ferroelectric polarization direction is changed, as shown in Figure 4(m)-(o).

We also find that the L-MOE can be effectively tuned by changing magnetization direction [see Figure 2(f)], which is strongly correlated to the valley polarization property since they all originate from the SOC effect. With the Néel vector \mathbf{n} rotating from the z -axis to the

- z -axis gradually, the L-MOE and valley-splitting ΔE_{valley} all display a period of 2π in θ . This can be understood from that the z component of spins at $\pi \pm \theta$ is the time-reversed counterpart of the one at θ and the L-MOE/ ΔE_{valley} is odd with respect to time-reversal symmetry \mathcal{T} . Especially, when the Néel vector is along the x direction, although the spin-splitting exists, while the valley-splitting is vanishing and L-MOE is thus prohibited [see Figure S6]. The underlining physics is that the system has a $\mathcal{O} = \mathcal{M}_x$ symmetry from magnetic point group of m when Néel vector $\mathbf{n}||x$. Because σ_{xy} is odd under \mathcal{M}_x symmetry, the L-MOE is expected to be zero. Thus, the predicted L-MOE is closely related to both the spin- and valley splitting, and it is characterized by the sign-reversible response controlled by ferroelectric polarization together with Néel vector directions.

Beyond the layer-stacking method, the L-MOE can be also facilitated even for \mathcal{TP} -symmetric AFMs (such as for bilayer Nb_3I_8 with AB stacking) via applying a static electric field, which can break the \mathcal{TP} symmetry and induce the spin-splitting.²⁵ The combined spin- and valley-splitting leads to the gate-controllable L-MOE [seeing Figures S10 and S16(a)]. Moreover, this field-driven L-MOE can be extended into a quantized version in antiferromagnetic Chern insulators, as done in bilayer MnBi_2Te_4 in the following discussion. It is known that the even-layer MnBi_2Te_4 ⁹⁴⁻⁹⁹ is a typical antiferromagnetic axion insulator with \mathcal{TP} -symmetric Kramers spin degeneracy, which provides a ideal platform for investigating the transport phenomena under the axion field $\mathbf{E}\cdot\mathbf{B}$ effect. *Gao et al.*²⁴ observed experimentally a fascinating type of Hall effect, coined layer Hall effect, in which the compensated layer-locked Berry curvature's contribution from top and bottom layer is broken and reversed by the axion field of $\mathbf{E}\cdot\mathbf{B}$. Our calculated layer Hall conductivity can reach the same order of the experimental report (*i.e.*, $0.5 e^2/h$)²⁴ at appropriate hole- or electron-doping, as shown in Figure S14. By extending the layer Hall effect into the ac case, it is natural to expect the sign-reversible L-MOE controlled by the electric field and Néel vector.

Interestingly, a novel topological phase transition is induced in bilayer MnBi_2Te_4 with the an increase of the electric field or SOC strength, as shown in Figure S13. Specially, a

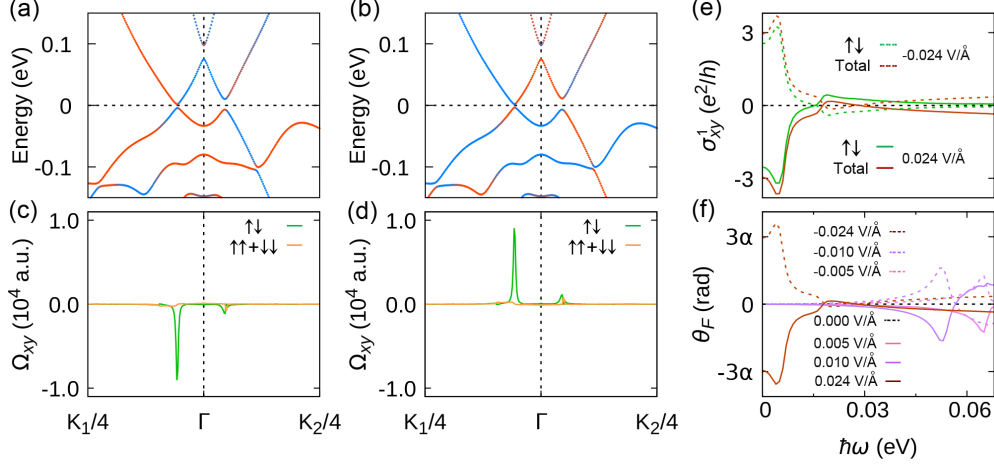


Figure 5: Sign-reversible quantum L-MOE in topological bilayer AFMs. (a, b) Band structure with SOC for bilayer MnBi_2Te_4 at $E = \pm 0.024 \text{ V/\AA}$. The colors denote the bands of the spin projection along the z direction. (c, d) Spin-resolved Berry curvature along symmetry lines at $E = \pm 0.024 \text{ V/\AA}$ from spin flip transition $\uparrow\downarrow$, and spin-conserved transition ($\uparrow\uparrow+\downarrow\downarrow$), respectively. (e) Spin-resolved optical Hall conductivity σ_{xy}^1 at $E = \pm 0.024 \text{ V/\AA}$ from spin flip transition $\uparrow\downarrow$, and the total contribution ($\uparrow\downarrow + \uparrow\uparrow + \downarrow\downarrow$), respectively. (f) L-MOE and its quantization of bilayer MnBi_2Te_4 at varying electric field.

Chern insulator phase emerges at a critical field of $E \approx 0.023 - 0.027 \text{ V/\AA}^{100}$ even without net magnetization. Because the role of SOC strength is closely related to the known Berry curvature (behaving like a fictitious magnetic field), the emergence of the topological phase transition may be traceable to the combined control by electric and magnetic field, which in fact has been first realized experimentally recently by Cai *et al.* in spin-canting MnBi_2Te_4 .¹⁰¹ The Chern insulator phase in bilayer MnBi_2Te_4 is characterized by a large quantized optical Hall conductivity in the low-frequency limit $\sigma_{xy}^1 = -3e^2/h$ [see Figure 5(e)]. As expected from the physics of layer Hall effect,²⁴ the quantized σ_{xy}^1 is also reversed by changing the electric field direction, which arises from the fact that the system at $E = \pm 0.024 \text{ V/\AA}$ hosts time-reversal-like degenerate spin-polarized electronic bands and the resulting opposite Berry curvatures, as shown in Figure 5(a)-(d). We also find that the large quantized σ_{xy}^1 is mainly contributed by the Berry curvature along the $\Gamma \rightarrow K_1$ direction [see Figure 5(c)-(d)], which is more than 4 orders of magnitude larger than that along the $\Gamma \rightarrow K_2$ direction, showing a valley-like polarized feature. Such a valley property, located at the general paths rather

than high-symmetry points, is also reported in few-layer transition metal dichalcogenides.¹⁰² Much interestingly, the Berry curvature and the σ_{xy}^1 mainly stem from the contribution from spin-flip transition [see Figure 5(c)-(e)] because the strong SOC-induced avoided crossings are separated between two bands with opposite spin states⁶⁶ [see Figure 5(a)-(b)]. Overall, the field effect shares the similar underlining physics as the above layer stacking effect, that is the spin-valley splitting in \mathcal{TP} -broken bilayer AFMs.

This spin-valley-polarized properties together with the topological properties ultimately give rise to the sign-reversible L-MOE in bilayer MnBi_2Te_4 [see Figure 5(f)]. In addition, the sign-reversible L-MOE is quantized in the low-frequency limit, *i.e.*, $\theta_K = -\tan^{-1}[c/(2\pi\sigma_{xy}^1)] \simeq \pm\pi/2$ [see Figure S16(b)] and $\theta_F = \tan^{-1}(2\pi\sigma_{xy}^1/c) \simeq C\alpha$ [see Figure 5(f)] (c is the speed of light, $C = \pm 3$ is the Chern number) due to the consideration from an axion term $(\Theta\alpha/4\pi^2)\mathbf{E}\cdot\mathbf{B}$ (here Θ is magnetoelectric polarizability and $\alpha = e^2/\hbar c$ is fine structure constant) into the usual Maxwell's equations.^{103–106} Thus, our findings are a crucial step for detecting experimentally this novel spin-valley polarized physics and the hidden topology simultaneously in such a large family of bilayer collinear AFMs by utilizing the noncontact modern magneto-optical technique.^{7,8,10–13}

In this study, using symmetry analyses and first-principles calculations, we proposed a novel class of magneto-optical interactions, namely L-MOE, which is rooted in the nontrivial combination of spin- and valley-splitting in bilayer AFMs. The L-MOE can be switched on/off by a layer-stacking effect or an electric field stimulus, originating from the uncompensated/compensated spin-conserving and spin-flip interband transitions. The key characteristic of L-MOE is the sign-reversible responses controlled by ferroelectric polarization, the Néel vector, or the electric field direction. Interestingly, the sign-reversible L-MOE can be quantized in topologically insulating AFMs. These findings promote our understanding of MOE in a large family of bilayer AFMs, and may have a potential impact in magneto-optical devices based on the novel layer, spin, and valley degrees of freedom.

Supporting Information Available

The Supporting Information contains: (a) the details of methods, (b) supplementary tables, figures, and discussions on other calculation results including different magnetic configurations, lattice constants, the dependence of Hubbard parameter U , band structures with different layer stacking and magnetization, transition between ferroelectric state and antiferroelectric state, (spin-resolved) optical conductivity with different layer stacking in bilayer Nb_3I_8 as well as the reduced coordinates for the Berry curvature slice, band structures and magneto-optical effects under electric fields, topological phase transition under different SOC and electric field strength, layer Hall conductivity and optical Hall conductivity in bilayer MnBi_2Te_4 .

Acknowledgement

The authors thank Wanxiang Feng, Li Feng, Run-Wu Zhang, Gui-Bin Liu, Ping Yang, and Libor Šmejkal for fruitful discussions. This work is supported by the National Natural Science Foundation of China (Grants Nos. 12304066, 12074154, 11722433, and 12174160), the Natural Science Foundation of Jiangsu Province (Grant No. BK20230684), the Natural Science Fund for Colleges and Universities in Jiangsu Province (Grant No. 23KJB140008), Six Talent Peaks Project and 333 High-level Talents Project of Jiangsu Province.

References

- (1) Kerr, J. On Rotation of the Plane of Polarization by Reflection from the Pole of a Magnet. *Phil. Mag.* **1877**, *3*, 321–343.
- (2) Faraday, M. I. Experimental Researches in Electricity.–Nineteenth Series. *Phil. Trans. R. Soc. Lond.* **1846**, *136*, 1–20.

- (3) Reim, W.; Schoenes, J. In *Handbook of Magnetic Materials*; Wohlfarth, E. P., Buschow, K. H. J., Eds.; Elsevier, New York, 1990; Vol. 5; Chapter 2.
- (4) Ebert, H. Magneto-Optical Effects in Transition Metal Systems. *Rep. Prog. Phys.* **1996**, *59*, 1665.
- (5) Antonov, V.; Harmon, B.; Yaresko, A. *Electronic Structure and Magneto-Optical Properties of Solids*; Kluwer Academic Publishers, Dordrecht, 2004; Chapter 1.4.
- (6) Kuch, W.; Schäfer, R.; Fischer, P.; Hillebrecht, F. U. *Magnetic Microscopy of Layered Structures*; Springer-Verlag Berlin Heidelberg, 2015; Chapter 2.
- (7) Huang, B.; Clark, G.; Navarro-Moratalla, E.; Klein, D. R.; Cheng, R.; Seyler, K. L.; Zhong, D.; Schmidgall, E.; McGuire, M. A.; Cobden, D. H.; Yao, W.; Xiao, D.; Jarillo-Herrero, P.; Xu, X. Layer-Dependent Ferromagnetism in a Van Der Waals Crystal down to the Monolayer Limit. *Nature* **2017**, *546*, 270–273.
- (8) Gong, C.; Li, L.; Li, Z.; Ji, H.; Stern, A.; Xia, Y.; Cao, T.; Bao, W.; Wang, C.; Wang, Y.; Qiu, Z. Q.; Cava, R. J.; Louie, S. G.; Xia, J.; Zhang, X. Discovery of Intrinsic Ferromagnetism in Two-Dimensional Van Der Waals Crystals. *Nature* **2017**, *546*, 265–269.
- (9) Deng, Y.; Yu, Y.; Song, Y.; Zhang, J.; Wang, N. Z.; Sun, Z.; Yi, Y.; Wu, Y. Z.; Wu, S.; Zhu, J.; Wang, J.; Chen, X. H.; Zhang, Y. Gate-tunable room-temperature ferromagnetism in two-dimensional Fe_3GeTe_2 . *Nature* **2018**, *563*, 94–99.
- (10) Wu, L.; Salehi, M.; Koirala, N.; Moon, J.; Oh, S.; Armitage, N. P. Quantized Faraday and Kerr Rotation and Axion Electrodynamics of a 3D Topological Insulator. *Science* **2016**, *354*, 1124–1127.
- (11) Okada, K. N.; Takahashi, Y.; Mogi, M.; Yoshimi, R.; Tsukazaki, A.; Takahashi, K. S.;

- Ogawa, N.; Kawasaki, M.; Tokura, Y. Terahertz Spectroscopy on Faraday and Kerr Rotations in a Quantum Anomalous Hall State. *Nat. Commun.* **2016**, *7*, 12245.
- (12) Shuvaev, A.; Dziom, V.; Kvon, Z. D.; Mikhailov, N. N.; Pimenov, A. Universal Faraday Rotation in HgTe Wells with Critical Thickness. *Phys. Rev. Lett.* **2016**, *117*, 117401.
- (13) Dziom, V.; Shuvaev, A.; Pimenov, A.; Astakhov, G. V.; Ames, C.; Bendias, K.; Böttcher, J.; Tkachov, G.; Hankiewicz, E. M.; Brüne, C.; Buhmann, H.; Molenkamp, L. W. Observation of the Universal Magnetoelectric Effect in a 3D Topological Insulator. *Nat. Commun.* **2017**, *8*, 15197.
- (14) Lee, J.; Mak, K. F.; Shan, J. Electrical Control of the Valley Hall Effect in Bilayer MoS₂ Transistors. *Nat. Nanotechnol.* **2016**, *11*, 421–425.
- (15) Lee, J.; Wang, Z.; Xie, H.; Mak, K. F.; Shan, J. Valley magnetoelectricity in single-layer MoS₂. *Nat. Mater.* **2017**, *16*, 887–891.
- (16) Feng, W.; Guo, G.-Y.; Zhou, J.; Yao, Y.; Niu, Q. Large Magneto-Optical Kerr Effect in Noncollinear Antiferromagnets Mn₃X ($X = \text{Rh}, \text{Ir}, \text{Pt}$). *Phys. Rev. B* **2015**, *92*, 144426.
- (17) Zhou, X.; Hanke, J.-P.; Feng, W.; Li, F.; Guo, G.-Y.; Yao, Y.; Blügel, S.; Mokrousov, Y. Spin-order Dependent Anomalous Hall Effect and Magneto-Optical Effect in the Noncollinear Antiferromagnets Mn₃XN with $X = \text{Ga}, \text{Zn}, \text{Ag}, \text{or Ni}$. *Phys. Rev. B* **2019**, *99*, 104428.
- (18) Wimmer, S.; Mankovsky, S.; Minár, J.; Yaresko, A. N.; Ebert, H. Magneto-Optic and Transverse-Transport Properties of Noncollinear Antiferromagnets. *Phys. Rev. B* **2019**, *100*, 214429.
- (19) Higo, T. et al. Large Magneto-Optical Kerr Effect and Imaging of Magnetic Octupole Domains in an Antiferromagnetic Metal. *Nat. Photonics* **2018**, *12*, 73–78.

- (20) Balk, A. L.; Sung, N. H.; Thomas, S. M.; Rosa, P. F. S.; McDonald, R. D.; Thompson, J. D.; Bauer, E. D.; Ronning, F.; Crooker, S. A. Comparing the Anomalous Hall Effect and the Magneto-Optical Kerr Effect through Antiferromagnetic Phase Transitions in Mn_3Sn . *Appl. Phys. Lett.* **2019**, *114*, 032401.
- (21) Wu, M.; Isshiki, H.; Chen, T.; Higo, T.; Nakatsuji, S.; Otani, Y. Magneto-Optical Kerr Effect in a Non-Collinear Antiferromagnet Mn_3Ge . *Appl. Phys. Lett.* **2020**, *116*, 132408.
- (22) Feng, W.; Hanke, J.-P.; Zhou, X.; Guo, G.-Y.; Blügel, S.; Mokrousov, Y.; Yao, Y. Topological Magneto-Optical Effects and Their Quantization in Noncoplanar Antiferromagnets. *Nat. Commun.* **2020**, *11*, 118.
- (23) Kato, Y. D.; Okamura, Y.; Hirschberger, M.; Tokura, Y.; Takahashi, Y. Topological magneto-optical effect from skyrmion lattice. *Nat. Commun.* **2023**, *14*, 5416.
- (24) Gao, A.; Liu, Y.-F.; Hu, C.; Qiu, J.-X.; Tzschaschel, C.; Ghosh, B.; Ho, S.-C.; Bérubé, D.; Chen, R.; Sun, H.; et al, Layer Hall effect in a 2D topological axion antiferromagnet. *Nature* **2021**, *595*, 521–525.
- (25) Sivadas, N.; Okamoto, S.; Xiao, D. Gate-Controllable Magneto-Optic Kerr Effect in Layered Collinear Antiferromagnets. *Phys. Rev. Lett.* **2016**, *117*, 267203.
- (26) Zhou, X.; Feng, W.; Yang, X.; Guo, G.-Y.; Yao, Y. Crystal chirality magneto-optical effects in collinear antiferromagnets. *Phys. Rev. B* **2021**, *104*, 024401.
- (27) Fan, F.-R.; Wu, H.; Nabok, D.; Hu, S.; Ren, W.; Draxl, C.; Stroppa, A. Electric-Magneto-Optical Kerr Effect in a Hybrid Organic–Inorganic Perovskite. *J. Am. Chem. Soc.* **2017**, *139*, 12883–12886.
- (28) Yang, K.; Hu, W.; Wu, H.; Whangbo, M.-H.; Radaelli, P. G.; Stroppa, A. Magneto-

- Optical Kerr Switching Properties of $(\text{CrI}_3)_2$ and $(\text{CrBr}_3/\text{CrI}_3)$ Bilayers. *ACS Appl. Electron. Mater.* **2020**, *2*, 1373–1380.
- (29) Samanta, K.; Ležaić, M.; Merte, M.; Freimuth, F.; Blügel, S.; Mokrousov, Y. Crystal Hall and Crystal Magneto-Optical Effect in Thin Films of SrRuO_3 . *J. Appl. Phys.* **2020**, *127*, 213904.
- (30) Mazin, I. I.; Koepernik, K.; Johannes, M. D.; González-Hernández, R.; Šmejkal, L. Prediction of unconventional magnetism in doped FeSb_2 . *Proc. Natl. Acad. Sci. U.S.A.* **2021**, *118*, e2108924118.
- (31) Wang, N.; Chen, J.; Ding, N.; Zhang, H.; Dong, S.; Wang, S.-S. Magneto-optical Kerr effect and magnetoelasticity in a weakly ferromagnetic RuF_4 monolayer. *Phys. Rev. B* **2022**, *106*, 064435.
- (32) Yananose, K.; Radaelli, P. G.; Cuoco, M.; Yu, J.; Stroppa, A. Activating magneto-electric optical properties by twisting antiferromagnetic bilayers. *Phys. Rev. B* **2022**, *106*, 184408.
- (33) Ding, N.; Yananose, K.; Rizza, C.; Fan, F.-R.; Dong, S.; Stroppa, A. Magneto-optical Kerr effect in ferroelectric antiferromagnetic two-dimensional heterostructures. *ACS Appl. Mater. Interfaces* **2023**, *15*, 22282–22290.
- (34) Xiao, D.; Yao, W.; Niu, Q. Valley-Contrasting Physics in Graphene: Magnetic Moment and Topological Transport. *Phys. Rev. Lett* **2007**, *99*, 236809.
- (35) Xiao, D.; Liu, G.-B.; Feng, W.; Xu, X.; Yao, W. Coupled Spin and Valley Physics in Monolayers of MoS_2 and Other Group-VI Dichalcogenides. *Phys. Rev. Lett* **2012**, *108*, 196802.
- (36) Xu, X.; Yao, W.; Xiao, D.; Heinz, T. F. Spin and Pseudospins in Layered Transition Metal Dichalcogenides. *Nat. Phys.* **2014**, *10*, 343–350.

- (37) Tong, W.-Y.; Gong, S.-J.; Wan, X.; Duan, C.-G. Concepts of Ferrovally Material and Anomalous Valley Hall Effect. *Nat. Commun* **2016**, *7*, 13612.
- (38) Mak, K. F.; Xiao, D.; Shan, J. Light-Valley Interactions in 2D Semiconductors. *Nat. Photonics* **2018**, *12*, 451–460.
- (39) Ma, H.-Y.; Hu, M.; Li, N.; Liu, J.; Yao, W.; Jia, J.-F.; Liu, J. Multifunctional antiferromagnetic materials with giant piezomagnetism and noncollinear spin current. *Nat. Commun.* **2021**, *12*, 2846.
- (40) Zhou, X.; Zhang, R.-W.; Zhang, Z.; Feng, W.; Mokrousov, Y.; Yao, Y. Sign-reversible valley-dependent Berry phase effects in 2D valley-half-semiconductors. *npj Comput. Mater.* **2021**, *7*, 160.
- (41) Liang, L.; Yang, Y.; Wang, X.; Li, X. Tunable Valley and Spin Splittings in VSi_2N_4 Bilayers. *Nano Lett.* **2023**, *23*, 858–862.
- (42) Yu, Z.-M.; Guan, S.; Sheng, X.-L.; Gao, W.; Yang, S. A. Valley-Layer Coupling: A New Design Principle for Valleytronics. *Phys. Rev. Lett* **2020**, *124*, 037701.
- (43) Ren, Y.; Ke, S.; Lou, W.-K.; Chang, K. Quantum phase transitions driven by sliding in bilayer MnBi_2Te_4 . *Phys. Rev. B* **2022**, *106*, 235302.
- (44) Chen, R.; Sun, H.-P.; Gu, M.; Hua, C.-B.; Liu, Q.; Lu, H.-Z.; Xie, X. C. Layer Hall effect induced by hidden Berry curvature in antiferromagnetic insulators. *Nat. Sci. Rev.* **2022**, *11*, nwac140.
- (45) Li, X.; Xu, X.; Zhou, H.; Jia, H.; Wang, E.; Fu, H.; Sun, J.-T.; Meng, S. Tunable Topological States in Stacked Chern Insulator Bilayers. *Nano Lett.* **2023**, *23*, 2839–2845.
- (46) Zhang, T.; Xu, X.; Huang, B.; Dai, Y.; Kou, L.; Ma, Y. Layer-polarized anomalous Hall effects in valleytronic van der Waals bilayers. *Mater. Horiz.* **2023**, *10*, 483–490.

- (47) Feng, Y.; Dai, Y.; Huang, B.; Kou, L.; Ma, Y. Layer Hall Effect in Multiferroic Two-Dimensional Materials. *Nano Lett.* **2023**, *23*, 5367–5372.
- (48) Peng, R.; Zhang, T.; He, Z.; Wu, Q.; Dai, Y.; Huang, B.; Ma, Y. Intrinsic layer-polarized anomalous Hall effect in bilayer MnBi_2Te_4 . *Phys. Rev. B* **2023**, *107*, 085411.
- (49) Huang, C.; Du, Y.; Wu, H.; Xiang, H.; Deng, K.; Kan, E. Prediction of Intrinsic Ferromagnetic Ferroelectricity in a Transition-Metal Halide Monolayer. *Phys. Rev. Lett.* **2018**, *120*, 147601.
- (50) Xu, M.; Huang, C.; Li, Y.; Liu, S.; Zhong, X.; Jena, P.; Kan, E.; Wang, Y. Electrical Control of Magnetic Phase Transition in a Type-I Multiferroic Double-Metal Trihalide Monolayer. *Phys. Rev. Lett.* **2020**, *124*, 067602.
- (51) Zhang, J.; Shen, X.; Wang, Y.; Ji, C.; Zhou, Y.; Wang, J.; Huang, F.; Lu, X. Design of Two-Dimensional Multiferroics with Direct Polarization-Magnetization Coupling. *Phys. Rev. Lett.* **2020**, *125*, 017601.
- (52) Liu, X.; Pyatakov, A. P.; Ren, W. Magnetoelectric Coupling in Multiferroic Bilayer VS_2 . *Phys. Rev. Lett.* **2020**, *125*, 247601.
- (53) Ji, J.; Yu, G.; Xu, C.; Xiang, H. J. General Theory for Bilayer Stacking Ferroelectricity. *Phys. Rev. Lett.* **2023**, *130*, 146801.
- (54) Tang, P.; Bauer, G. E. W. Sliding Phase Transition in Ferroelectric van der Waals Bilayers. *Phys. Rev. Lett.* **2023**, *130*, 176801.
- (55) Wu, Y.; Tong, J.; Deng, L.; Luo, F.; Tian, F.; Qin, G.; Zhang, X. Coexisting Ferroelectric and Ferrovalley Polarizations in Bilayer Stacked Magnetic Semiconductors. *Nano Lett.* **2023**, *23*, 6226–6232.

- (56) Šmejkal, L.; Sinova, J.; Jungwirth, T. Beyond Conventional Ferromagnetism and Antiferromagnetism: A Phase with Nonrelativistic Spin and Crystal Rotation Symmetry. *Phys. Rev. X* **2022**, *12*, 031042.
- (57) Šmejkal, L.; Sinova, J.; Jungwirth, T. Emerging Research Landscape of Altermagnetism. *Phys. Rev. X* **2022**, *12*, 040501.
- (58) Zhou, X.; Feng, W.; Zhang, R.-W.; Šmejkal, L.; Sinova, J.; Mokrousov, Y.; Yao, Y. Crystal Thermal Transport in Altermagnetic RuO₂. *Phys. Rev. Lett.* **2024**, *132*, 056701.
- (59) Weaver, J. H.; Colavita, E.; Lynch, D. W.; Rosei, R. Low-energy interband absorption in bcc Fe and hcp Co. *Phys. Rev. B* **1979**, *19*, 3850–3856.
- (60) Marusak, L. A.; Messier, R.; White, W. B. Optical absorption spectrum of hematite, $\alpha\text{Fe}_2\text{O}_3$ near IR to UV. *J. Phys. Chem. Solids* **1980**, *41*, 981–984.
- (61) Khazan, L. S.; Rubo, Y. G.; Sheka, V. I. Exchange-induced optical spin transitions in semimagnetic semiconductors. *Phys. Rev. B* **1993**, *47*, 13180–13188.
- (62) Sexton, J. H.; Lynch, D. W.; Benbow, R. L.; Smith, N. V. Empirical band calculations of the optical properties of d-band metals. VI. The optical conductivity of ferromagnetic iron. *Phys. Rev. B* **1988**, *37*, 2879–2883.
- (63) Hoerstel, W.; Kraak, W.; Masselink, W. T.; Mazur, Y. I.; Tarasov, G. G.; Kuzmenko, E. V.; Tomm, J. W. Spin-flip effects in the magnetoluminescence and magnetoresistance of semimagnetic narrow-gap $\text{Hg}_{1-x-y}\text{Cd}_x\text{Mn}_y\text{Te}$. *Phys. Rev. B* **1998**, *58*, 4531–4537.
- (64) Zhang, H.; Freimuth, F.; Blügel, S.; Mokrousov, Y.; Souza, I. Role of Spin-Flip Transitions in the Anomalous Hall Effect of FePt Alloy. *Phys. Rev. Lett.* **2011**, *106*, 117202.

- (65) Ezawa, M. Spin-valley optical selection rule and strong circular dichroism in silicene. *Phys. Rev. B* **2012**, *86*, 161407.
- (66) Gibertini, M.; Pellegrino, F. M. D.; Marzari, N.; Polini, M. Spin-resolved optical conductivity of two-dimensional group-VIB transition-metal dichalcogenides. *Phys. Rev. B* **2014**, *90*, 245411.
- (67) Brotons-Gisbert, M.; Baek, H.; Molina-Sánchez, A.; Campbell, A.; Scerri, E.; White, D.; Watanabe, K.; Taniguchi, T.; Bonato, C.; Gerardot, B. D. Spin-layer locking of interlayer excitons trapped in moiré potentials. *Nature Materials* **2020**, *19*, 630–636.
- (68) Simon, A.; Von Schnering, H. G. β -Nb₃Br₈ und β -Nb₃I₈ darstellung, eigenschaften und struktur. *Journal of the Less Common Metals* **1966**, *11*, 31–46.
- (69) Magonov, S. N.; Zoennchen, P.; Rotter, H.; Cantow, H. J.; Thiele, G.; Ren, J.; Whangbo, M. H. Scanning tunneling and atomic force microscopy study of layered transition metal halides Nb₃X₈ (X = Cl, Br, I). *J. Am. Chem. Soc.* **1993**, *115*, 2495–2503.
- (70) Kim, B. J. et al. Structural and Electrical Properties of Nb₃I₈ Layered Crystal. *Phys. Status Solidi RRL* **2018**, *13*, 1800448.
- (71) Oh, S.; Choi, K. H.; Chae, S.; Kim, B. J.; Jeong, B. J.; Lee, S. H.; Jeon, J.; Kim, Y.; Nanda, S. S.; Shi, L.; et al, Large-area synthesis of van der Waals two-dimensional material Nb₃I₈ and its infrared detection applications. *J. Alloy. Compd.* **2020**, *831*, 154877.
- (72) Jiang, J.; Liang, Q.; Meng, R.; Yang, Q.; Tan, C.; Sun, X.; Chen, X. Exploration of new ferromagnetic, semiconducting and biocompatible Nb₃X₈ (X= Cl, Br or I) monolayers with considerable visible and infrared light absorption. *Nanoscale* **2017**, *9*, 2992–3001.

- (73) Peng, R.; Ma, Y.; Xu, X.; He, Z.; Huang, B.; Dai, Y. Intrinsic Anomalous Valley Hall Effect in Single-Layer Nb₃I₈. *Phys. Rev. B* **2020**, *102*, 035412.
- (74) Conte, F.; Ninno, D.; Cantele, G. Layer-dependent electronic and magnetic properties of Nb₃I₈. *Phys. Rev. Research* **2020**, *2*, 033001.
- (75) Cantele, G.; Conte, F.; Zullo, L.; Ninno, D. Tunable electronic and magnetic properties of thin Nb₃I₈ nanofilms: Interplay between strain and thickness. *Phys. Rev. B* **2022**, *106*, 085418.
- (76) Duan, J.; Ma, D.-S.; Zhang, R.-W.; Jiang, W.; Zhang, Z.; Cui, C.; Yu, Z.-M.; Yao, Y. Cataloging High-Quality Two-Dimensional van der Waals Materials with Flat Bands. *Adv. Funct. Mater.* **2024**, 2313067.
- (77) Feng, L.; Chen, X.; Qi, J. Nonvolatile electric field control of spin-valley-layer polarized anomalous Hall effect in a two-dimensional multiferroic semiconductor bilayer. *Phys. Rev. B* **2023**, *108*, 115407.
- (78) Hong, J.; Sui, F.; Wang, K.; Han, X.; Zheng, Y.; Tong, W.-y.; Deng, X.; Guan, Z.; Tian, B.; et al, Coexistence of chiral phonons and antiferroelectricity in breathing kagome semiconductor Nb₃I₈ at room-temperature. <https://doi.org/10.21203/rs.3.rs-3457733/v1> **2023**,
- (79) Regmi, S.; Fernando, T.; Zhao, Y.; Sakhya, A. P.; Dhakal, G.; Elius, I. B.; Vazquez, H.; Denlinger, J. D.; Yang, J.; Chu, J.-H.; Xu, X.; Cao, T.; Neupane, M. Spectroscopic evidence of flat bands in breathing kagome semiconductor Nb₃I₈. *Commun Mater* **2022**, *3*, 100.
- (80) Regmi, S. et al. Observation of flat and weakly dispersing bands in the van der Waals semiconductor Nb₃Br₈ with breathing kagome lattice. *Phys. Rev. B* **2023**, *108*, L121404.

- (81) Zhang, Y.; Gu, Y.; Weng, H.; Jiang, K.; Hu, J. Mottness in two-dimensional van der Waals Nb_3X_8 monolayers ($X = \text{Cl}, \text{Br}, \text{I}$). *Phys. Rev. B* **2023**, *107*, 035126.
- (82) Gao, S. et al. Discovery of a Single-Band Mott Insulator in a van der Waals Flat-Band Compound. *Phys. Rev. X* **2023**, *13*, 041049.
- (83) Sivadas, N.; Okamoto, S.; Xu, X.; Fennie, C. J.; Xiao, D. Stacking-Dependent Magnetism in Bilayer CrI_3 . *Nano Lett.* **2018**, *18*, 7658–7664.
- (84) Gudelli, V. K.; Guo, G.-Y. Magnetism and magneto-optical effects in bulk and few-layer CrI_3 : a theoretical GGA+ U study. *New J. Phys.* **2019**, *21*, 053012.
- (85) Fang, Y.; Wu, S.; Zhu, Z.-Z.; Guo, G.-Y. Large magneto-optical effects and magnetic anisotropy energy in two-dimensional $\text{Cr}_2\text{Ge}_2\text{Te}_6$. *Phys. Rev. B* **2018**, *98*, 125416.
- (86) Yang, X.; Zhou, X.; Feng, W.; Yao, Y. Strong magneto-optical effect and anomalous transport in the two-dimensional van der Waals magnets Fe_nGeTe_2 ($n = 3, 4, 5$). *Phys. Rev. B* **2021**, *104*, 104427.
- (87) Yang, X.; Zhou, X.; Feng, W.; Yao, Y. Tunable magneto-optical effect, anomalous Hall effect, and anomalous Nernst effect in the two-dimensional room-temperature ferromagnet $1T$ - CrTe_2 . *Phys. Rev. B* **2021**, *103*, 024436.
- (88) Yang, X.; Yang, P.; Zhou, X.; Feng, W.; Yao, Y. First- and second-order magneto-optical effects and intrinsically anomalous transport in the two-dimensional van der Waals layered magnets CrXY ($X = \text{S}, \text{Se}, \text{Te}; Y = \text{Cl}, \text{Br}, \text{I}$). *Phys. Rev. B* **2022**, *106*, 054408.
- (89) Li, X.; Cao, T.; Niu, Q.; Shi, J.; Feng, J. Coupling the Valley Degree of Freedom to Antiferromagnetic Order. *Proc. Natl. Acad. Sci. (USA)* **2013**, *110*, 3738–3742.
- (90) Cui, Q.; Zhu, Y.; Liang, J.; Cui, P.; Yang, H. Spin-valley coupling in a two-dimensional VSi_2N_4 monolayer. *Phys. Rev. B* **2021**, *103*, 085421.

- (91) Feng, X.; Xu, X.; He, Z.; Peng, R.; Dai, Y.; Huang, B.; Ma, Y. Valley-related multiple Hall effect in monolayer VSi_2P_4 . *Phys. Rev. B* **2021**, *104*, 075421.
- (92) Zhan, F.; Zeng, J.; Chen, Z.; Jin, X.; Fan, J.; Chen, T.; Wang, R. Floquet Engineering of Nonequilibrium Valley-Polarized Quantum Anomalous Hall Effect with Tunable Chern Number. *Nano Lett.* **2023**, *23*, 2166–2172.
- (93) Guo, S.-D.; Tao, Y.-L.; Guo, H.-T.; Zhao, Z.-Y.; Wang, B.; Wang, G.; Wang, X. Possible electronic state quasi-half-valley metal in a VGe_2P_4 monolayer. *Phys. Rev. B* **2023**, *107*, 054414.
- (94) Li, J.; Li, Y.; Du, S.; Wang, Z.; Gu, B.-L.; Zhang, S.-C.; He, K.; Duan, W.; Xu, Y. Intrinsic Magnetic Topological Insulators in Van Der Waals Layered MnBi_2Te_4 -Family Materials. *Sci. Adv.* **2019**, *5*, eaaw5685.
- (95) Otrokov, M. M.; Rusinov, I. P.; Blanco-Rey, M.; Hoffmann, M.; Vyazovskaya, A. Y.; Ereemeev, S. V.; Ernst, A.; Echenique, P. M.; Arnau, A.; Chulkov, E. V. Unique Thickness-Dependent Properties of the Van Der Waals Interlayer Antiferromagnet MnBi_2Te_4 Films. *Phys. Rev. Lett.* **2019**, *122*, 107202.
- (96) Zhang, D.; Shi, M.; Zhu, T.; Xing, D.; Zhang, H.; Wang, J. Topological Axion States in the Magnetic Insulator MnBi_2Te_4 with the Quantized Magnetoelectric Effect. *Phys. Rev. Lett.* **2019**, *122*, 206401.
- (97) Liu, C.; Wang, Y.; Li, H.; Wu, Y.; Li, Y.; Li, J.; He, K.; Xu, Y.; Zhang, J.; Wang, Y. Robust Axion Insulator and Chern Insulator Phases in a Two-dimensional Antiferromagnetic Topological Insulator. *Nat. Mater.* **2020**, *19*, 522–527.
- (98) Deng, Y.; Yu, Y.; Shi, M. Z.; Guo, Z.; Xu, Z.; Wang, J.; Chen, X. H.; Zhang, Y. Quantum anomalous Hall effect in intrinsic magnetic topological insulator MnBi_2Te_4 . *Science* **2020**, *367*, 895–900.

- (99) Ge, J.; Liu, Y.; Li, J.; Li, H.; Luo, T.; Wu, Y.; Xu, Y.; Wang, J. High-Chern-number and high-temperature quantum Hall effect without Landau levels. *Natl. Sci. Rev.* **2020**, *7*, 1280–1287.
- (100) Du, S.; Tang, P.; Li, J.; Lin, Z.; Xu, Y.; Duan, W.; Rubio, A. Berry curvature engineering by gating two-dimensional antiferromagnets. *Phys. Rev. Research* **2020**, *2*, 022025.
- (101) Cai, J.; Ovchinnikov, D.; Fei, Z.; He, M.; Song, T.; Lin, Z.; Wang, C.; Cobden, D.; Chu, J.-H.; Cui, Y.-T.; et al, Electric control of a canted-antiferromagnetic Chern insulator. *Nat. Commun.* **2022**, *13*, 1668.
- (102) Wu, Z.; Xu, S.; Lu, H.; Khamoshi, A.; Liu, G.-B.; Han, T.; Wu, Y.; Lin, J.; Long, G.; He, Y.; et al, Even–odd layer-dependent magnetotransport of high-mobility Q-valley electrons in transition metal disulfides. *Nat. Commun.* **2016**, *7*, 12955.
- (103) Qi, X.-L.; Hughes, T. L.; Zhang, S.-C. Topological Field Theory of Time-reversal Invariant Insulators. *Phys. Rev. B* **2008**, *78*, 195424.
- (104) Maciejko, J.; Qi, X.-L.; Drew, H. D.; Zhang, S.-C. Topological Quantization in Units of the Fine Structure Constant. *Phys. Rev. Lett.* **2010**, *105*, 166803.
- (105) Tse, W.-K.; MacDonald, A. H. Giant Magneto-Optical Kerr Effect and Universal Faraday Effect in Thin-Film Topological Insulators. *Phys. Rev. Lett.* **2010**, *105*, 057401.
- (106) Tse, W.-K.; MacDonald, A. H. Magneto-optical Faraday and Kerr effects in Topological Insulator Films and in other Layered Quantized Hall Systems. *Phys. Rev. B* **2011**, *84*, 205327.

Graphical TOC Entry

